MIT Libraries | DSpace@MIT

MIT Open Access Articles

Non-monotonic effect of growth temperature on carrier collection in SnS solar cells

The MIT Faculty has made this article openly available. ***Please share*** how this access benefits you. Your story matters.

Citation: Chakraborty, R. et al. "Non-Monotonic Effect of Growth Temperature on Carrier Collection in SnS Solar Cells." Applied Physics Letters 106, 20 (May 2015): 203901 © 2015 AIP Publishing LLC

As Published: http://dx.doi.org/10.1063/1.4921326

Publisher: AIP Publishing

Persistent URL: http://hdl.handle.net/1721.1/118303

Version: Author's final manuscript: final author's manuscript post peer review, without publisher's formatting or copy editing

Terms of use: Creative Commons Attribution-Noncommercial-Share Alike

Massachusetts Institute of Technology

Non-monotonic effect of growth temperature on carrier collection in SnS solar cells

R. Chakraborty,[1] V. Steinmann, [1] N. M. Mangan, [1] R. E. Brandt, [1] J. R. Poindexter, [1] R. Jaramillo, [1] J. P. Mailoa, [1] K. Hartman, [1] A. Polizzotti, [1] C. Yang, [2] R. G. Gordon, [2] T. Buonassisi,[1]

[1]*Massachusetts Institute of Technology, Cambridge, MA, 02139, USA*

[2]*Harvard University, Cambridge, MA, 02138, USA*

We quantify the effects of growth temperature on material and device properties of thermally evaporated SnS thin-films and test structures. Grain size, Hall mobility, and majority-carrier concentration monotonically increase with growth temperature. However, the charge collection as measured by the long-wavelength contribution to short-circuit current exhibits a non-monotonic behavior: the collection decreases with increased growth temperature from 150°C to 240°C and then recovers at 285°C. Fits to the experimental internal quantum efficiency using an opto-electronic model indicate that the non-monotonic behavior of charge-carrier collection can be explained by a transition from drift- to diffusion-assisted components of carrier collection. The results show a promising increase in the extracted minority-carrier diffusion length at the highest growth temperature of 285°C. These findings illustrate how coupled mechanisms can affect early-stage device development, highlighting the critical role of direct materials property measurements and simulation.

Tin (II) sulfide (SnS) is a promising Earth-abundant thin-film solar absorber material because of its high absorption coefficient in the visible wavelengths,[1–5] tunable hole carrier density in the range 10^{15} to 10^{18} cm^{-3},[1,6] and potential for high-throughput manufacturing.[5] In recent years, the conversion efficiency of SnS-based solar cells has considerably improved from 1.3% to 4.36%.[1,7–11] However, the record efficiency still pales in comparison to the theoretical maximum efficiency[a] of SnS, 32%.[12] As a step towards understanding the loss mechanisms at play, the present work focuses on the measurement and modeling of carrier collection and photocurrent in SnS devices. The methodology used here to connect material properties to device performance generalizes to other thin-film absorber materials in early-stage device development.

We recently reported on thermally evaporated SnS-based solar cells with a short-circuit current (J_{SC}) of 20.6 mA/cm^2.[5] This is among the highest J_{SC} in the literature for SnS-based solar cells,[10,11] yet is still less than half of the theoretical maximum of 43.3 mA/cm^2.[5] An analysis of the external quantum efficiency revealed the leading loss mechanism: 19% of all incident photons are lost to recombination, mostly at long wavelengths (>700 nm).[5] Improving charge-carrier collection in the SnS layer is a critical step toward improving the short-circuit current to levels that justify industrial scale-up.

For other thermally evaporated thin-film solar cell materials such as cadmium telluride and copper (indium, gallium) (diselenide, disulfide), the growth temperature T_g is a critical process parameter affecting charge-carrier collection in devices.[13,14] Although the effect of T_g on crystalline texture, grain size, electrical transport properties, and optical properties of SnS thin films has been studied extensively,[15–19] its effect on charge-carrier collection has not yet been directly measured through a working SnS photovoltaic device.

[a] Assumes a bandgap of 1.1 eV.

In this work, we determine the effect of growth temperature T_g on the structural and electrical properties of thermally evaporated SnS films. We then measure the internal quantum efficiency (IQE) of devices using a previously developed device stack.[5] IQE probes the collection efficiency due to drift and diffusion, allowing us to analyze the transport properties of SnS under different processing conditions. By increasing the SnS growth temperature from 150 to 285°C, we traverse through a local minimum in long-wavelength carrier collection, a behavior we attribute to the combined effects of a varying SnS majority-carrier concentration and minority-carrier diffusion length. A monotonic increase in carrier concentration with increasing growth temperature leads to decreasing drift-assisted carrier collection. This causes a decrease in total collection up to the highest growth temperature of 285°C. Despite the decrease in drift-assisted collection at 285°C, we see a recovery in total long-wavelength carrier collection due to an improvement in minority-carrier diffusion length. This suggests that the films grown at the highest temperature have a lower density of lifetime-limiting bulk defects.

The SnS thin films are grown via thermal evaporation on Si/SiO_2/Mo substrates at four substrate temperatures: 150, 200, 240, and 285°C. The deposition rate is held at 1–2 Å/s. Substrate temperatures higher than 285°C result in re-evaporation of SnS from the substrate due to the low deposition rate and large source-to-substrate distance (10 cm) in our thermal evaporation system. All films are subsequently annealed at 400°C in 4% H_2S atmosphere (N_2 balance) at 28 Torr for 60 minutes to promote grain growth. Re-evaporation is strongly suppressed during annealing,[20] presumably because the high total pressure limits re-evaporation. The post-annealed film thicknesses range from 886-1204 nm due to differences in surface topology and error in deposition rate measurement. Devices are fabricated with each annealed film using a previously reported procedure.[21] The device stack includes a thin SnO_2 layer on the SnS surface and a Zn(O,S):N *n*-type buffer layer. Each sample contains 11 devices defined by a shadow-masked ITO pattern. Further details on the preparation of SnS powder, preparation of

$Si/SiO_2/Mo$ substrates, thermal evaporation and annealing parameters, and device fabrication steps are described in prior work.[21]

We first study the impact of T_g on the structural and electronic properties of SnS thin-films, summarized in Figure 1. The morphology of the SnS films are characterized by field-emission scanning electron microscopy (Zeiss, Ultra-55), and grain areas are extracted by analyzing manual traces[20] using the image processing software ImageJ.[22] The micrographs (Figure 1a) indicate a variation in packing density of grains. As T_g increases, intergranular voids decrease in size and frequency. Figure 1b shows a box plot representing the distribution of in-plane grain diameters (assuming circular grains) for each growth temperature. The median grain diameter increases monotonically with T_g, ranging from 191 nm at $T_g = 150°C$ to 383 nm at $T_g = 285°C$. The grain diameter distribution profile also changes as a function of T_g. As T_g increases, the midspread of grain diameters increases, accompanied by an increasingly positive skew in the distribution. For example, the upper quartile grain size for $T_g = 150°C$ is 269 nm, as compared to 616 nm for $T_g = 285°C$. All of these morphological trends are observed despite an identical 1-hr post-deposition anneal at 400°C for all samples. This suggests that the as-grown film morphology may kinetically limit the grain-growth during the subsequent anneal step.

Figure 1c and 1d show the results of Hall effect measurements carried out on SnS sister samples grown on Si/SiO_2 wafers. All films were *p*-type, and the hole concentration increased monotonically with T_g from 6.3×10^{15} to 3.1×10^{16} cm^{-3}. The hole concentration is likely controlled by the concentration of doubly-ionized Sn vacancies, which are predicted to be shallow acceptors.[23] The film resistivity decreased from 49 to 6.3 Ω-cm. Hole mobility tended to increase with T_g, ranging from 20.1 to 31.6 $cm^2/V \cdot s$. The upward trend in grain size and mobility with T_g is consistent with decreasing grain boundary scattering,[24] but other intragranular scattering processes may also limit mobility. Notably, the dependence of electrical properties on T_g persist despite a post-deposition anneal at 400°C.

External quantum efficiency measurements are performed (PV Measurements Model QEX7) at room temperature without light or voltage bias. Internal quantum efficiency is calculated by $\mathrm{IQE} = \frac{\mathrm{EQE}}{1-R}$, where R is the reflectivity of the device stack as measured by a spectrophotometer (Perkins Elmer Lambda 950). Figure 2 shows the average IQE from all rectifying devices on each substrate. Below 450 nm, the IQE drops sharply due to optical absorption in the Zn(O,S):N and ITO layers.[5] In the wavelength range 450-700 nm, the IQE varies across growth temperatures. Although this short-wavelength region is sensitive to carrier collection within 100 nm from the SnS/Zn(O,S):N interface (as $\alpha > 10^5$ $\mathrm{cm^{-1}}$ for these wavelengths), this region is also particularly sensitive to errors in the reflectivity measurement due to pronounced optical interference in the ITO and Zn(O,S):N layers. In contrast, the long-wavelength region 700-950 nm is more sensitive to changes in carrier collection throughout the bulk, because for these wavelengths the absorption coefficient α is as low as 10^4 $\mathrm{cm^{-1}}$ and film thicknesses are $\sim 10^{-4}$ cm. Moreover, interference fringes in the reflectivity spectrum due to the ITO and Zn(O,S):N layers are less pronounced for wavelengths beyond 700 nm. Thus, we restrict our analysis of carrier collection to the long-wavelength region 700-950 nm. In this region, we observe an unexpected trend: the magnitude of IQE varies non-monotonically with T_g. Figure 3a shows the integrated IQE in the long-wavelength range in terms of the current density

$$J_{\mathrm{IQE,lw}} = \int_{700\ \mathrm{nm}}^{950\ \mathrm{nm}} \mathrm{IQE}(\lambda)\ \phi_{AM1.5}(\lambda)\ \frac{\lambda}{hc}\ d\lambda \tag{1}$$

where $\phi_{AM1.5}(\lambda)$ is the AM1.5 spectral irradiance. As growth temperature increases, $J_{\mathrm{IQE,lw}}$ decreases from 8.4 mA/cm^2 at $T_\mathrm{g} = 150°\mathrm{C}$, to 6.3 mA/cm^2 at $T_\mathrm{g} = 240°\mathrm{C}$, and then increases back to 8.4 mA/cm^2 at the highest growth temperature of 285°C (Figure 3a).

We hypothesize that this non-monotonic behavior in long-wavelength IQE with temperature is due to the combined effects of a varying majority-carrier (hole) concentration p and minority-carrier diffusion length L_{diff}. The depletion width decreases with increasing p, reducing the distance over which the

internal electric field assists collection of minority electrons from the SnS bulk. That is, a lower hole concentration should result in a larger photo-generated carrier collection because there is a higher minority-carrier drift current. Figure 3b shows the depletion widths computed using measured hole carrier concentrations and an analytic expression for heterojunctions.[20,25] The SnS film grown at the lowest temperature of 150°C has the lowest p (Figure 1d), the largest depletion width, and thus the most drift-assisted collection. As carrier concentration increases with T_{g}, we expect a decrease in drift-assisted collection due to a shrinking depletion width. This trend in expected drift-assisted collection is consistent with the trend in $J_{\mathrm{IQE,lw}}$ for $T_g \leq 240$°C. However, for the highest growth temperature of 285°C, we observe a recovery of $J_{\mathrm{IQE,lw}}$ despite the relatively small depletion width. One possible mechanism for the relatively high $J_{\mathrm{IQE,lw}}$ at 285°C is by an enhancement of L_{diff}.

We verify this hypothesis by implementing a one-dimensional opto-electronic model in SCAPS-1D[26] and fitting to the experimental long-wavelength IQE.[20] With the model, we demonstrate that the decreasing trend in $J_{\mathrm{IQE,lw}}$ for growth temperatures up to 240°C is caused by an increasing hole concentration, while the resurgence in $J_{\mathrm{IQE,lw}}$ at 285°C is driven by an increase in L_{diff}. As inputs to the simulation, we use material parameters extracted from experimental data on the here-studied samples in conjunction with literature values.[20] Within the defined parameter space, the minority-carrier mobility μ_e and minority-carrier lifetime τ_n affect $J_{\mathrm{IQE,lw}}$ equivalently. We aim to fit the simulated long-wavelength (700–950 nm) IQE to experimental data by using the $\mu_e \tau_n$ product as the effective fitting parameter, and then extract the fitted diffusion length $L_{\mathrm{diff}} = \sqrt{\frac{kT}{q}\mu_e \tau_n}$.[20]

The fitted diffusion lengths are shown by the filled squares in Figure 3c. The error bars in Figure 3c take into account both uncertainty in material parameters from the literature, as well as the effect of varying T_{g}-dependent parameters other than hole concentration.[20] For the lowest growth temperature of 150°C, the fitted diffusion length ranges from 88−135 nm. Remarkably, the L_{diff} ranges for $T_{\mathrm{g}} = 200$°C and

240°C statistically overlap with the range for $T_g = 150°C$, implying that the change in hole concentration alone is sufficient to explain the change in $J_{IQE,lw}$ for growth temperatures up to 240°C. However, the fitted diffusion lengths for T_g =285°C range from 172–228 nm, well above the ranges for lower growth temperatures. Thus, even accounting for variation of other parameters, the recovery in $J_{IQE,lw}$ at $T_g = 285°C$ cannot be explained without an increase in L_{diff} of the films deposited at this temperature. We note that the hole concentration measurements are performed on different substrates from those used for device measurements. Although this could result in quantitative differences in p and the fitted L_{diff}, the trends in p and L_{diff} as a function of T_g are likely unaffected.[20] As a check, we also consider the effects of a varying surface roughness and absorption coefficient on $J_{IQE,lw}$, and find that they are insufficient to account for the variation in measured $J_{IQE,lw}$.[20]

Because the Hall mobility increases by only 2.9% from T_g = 240°C to 285°C, the rise in L_{diff} at 285°C is likely driven by an enhancement of effective minority-carrier lifetime. Recalling that the grain size is highest for T_g = 285°C, a reduction in grain boundary recombination may contribute to the increase in L_{diff}.[27] However, grain size tends to increase monotonically with temperature, whereas the fitted L_{diff} stays nearly constant for $T_g < 285°C$. Thus, grain boundary recombination alone does not explain the trend in fitted L_{diff} . Instead, we suspect that a reduction of intragranular defect density is responsible for the enhancement of minority-carrier lifetime at $T_g = 285°C$.

In optimizing SnS bulk properties for maximum carrier collection, we would ideally benefit from both drift and diffusion. Figure 4 is a contour plot of simulated $J_{IQE,lw}$ for a range of SnS hole concentrations and diffusion lengths, with the results of the present study appropriately overlayed in the parameter space.[20] Here it is more easily seen how as T_g increases, we traverse through the parameter space in a way that produces lower $J_{IQE,lw}$ at the intermediate temperatures. Additionally, we should aim for both lower carrier concentrations (towards 10^{15} cm^{-3}) and higher diffusion lengths to achieve long-

wavelength current densities approaching the theoretical maximum of $J_{\mathrm{IQE,lw}} = 15.0$ mA/cm^2. It is also important to note a qualitative difference in the effect of hole concentration versus that of diffusion length on $J_{\mathrm{IQE,lw}}$. Increasing L_{diff} increases both diffusive and drift collection and is especially effective at improving carrier collection. In contrast, decreasing p can only increase collection by enlarging the depletion region and has a more limited improvement capacity. As the carrier concentration is decreased, the loss in current due to the series resistance of SnS counteracts the benefit of drift-assisted collection. Consequently, for a given diffusion length, the net benefit of decreasing p diminishes as p is lowered. We note that while the IQE measurements focus exclusively on the short-circuit point, the SnS hole concentration also affects the open-circuit voltage and fill factor. The SnS hole concentration should thus be optimized not only for short-circuit carrier collection, but for overall device efficiency. Work is ongoing in co-optimizing growth and annealing conditions to allow tunable carrier concentration while maximizing diffusion lengths.

In summary, we have shown that by increasing growth temperature from 150 to 285°C, we traverse through a local minimum in current density at long wavelengths due to the combined effects of a varying carrier concentration and diffusion length. The hole concentration monotonically increases with increasing growth temperature, which leads to decreasing drift-assisted carrier collection. At the highest growth temperature, we observe a recovery of the carrier collection due to an increase in diffusive minority-carrier transport. Higher carrier collection may be achievable by simultaneously decreasing carrier concentration and increasing diffusion length. The fact that the trends in grain morphology, carrier concentration, and extracted diffusion length are observed after a post-growth annealing step of 400°C in H_2S ambient highlights the importance of defect engineering during thin-film growth to achieve optimum bulk material properties. The increase in diffusive carrier transport at 285°C is promising, as it suggests we may achieve even higher diffusion lengths and enhanced device performance with growth temperatures beyond 285°C. Higher substrate temperatures can be attained by

increasing the source temperature and decreasing the source-substrate distance to increase the SnS adatom flux. Ideally, a close-space sublimation geometry would be employed, allowing far higher growth temperatures. These steps to increase growth temperature may be critical to achieve high-quality SnS thin films which ultimately improve the efficiency of SnS-based photovoltaic devices.

Acknowledgements

The authors are thankful to Mariela Lizet Castillo for helping with substrate preparation. The authors also thank Luisa Barrera and Kelsey Doolittle for helping with the grain size analysis and anisotropic calculations, respectively. This work is supported by the U.S. Department of Energy through the SunShot Initiative under contract DE-EE0005329, and by Robert Bosch LLC through the Bosch Energy Research Network under grant 02.20.MC11. V. Steinmann, R. Jaramillo, K. Hartman, and R.E. Brandt acknowledge the support of the Alexander von Humboldt foundation, a DOE EERE Postdoctoral Research Award, an Intel PhD Fellowship, and an NSF GRFP Fellowship respectively. This work made use of the MRSEC Shared Experimental Facilities at MIT that is supported by the National Science Foundation (NSF) under award DMR-08-19762, and the Center for Nanoscale Systems that is supported by the NSF under award ECS-0335765.

RC led the experimental planning, film characterization, and data analysis. VS aided in experimental planning, sample fabrication, and device characterization. RC, VS, NMM, and REB wrote the paper. JRP took the IQE data and helped with initial IQE analysis which led to the full device simulations. NMM and REB assisted with the device simulations and interpretation of the simulation results. RJ carried out the AFM measurements, helped interpret the 2D optical simulation results, and contributed to device fabrication. JPM carried out the 2D optical simulations. KH, AP, and CY were involved with sample fabrication. RGG and TB led the overall project as the PIs of the collaborating labs at Harvard and MIT, including assisting the team with data interpretation, structuring, and presentation.

Figures

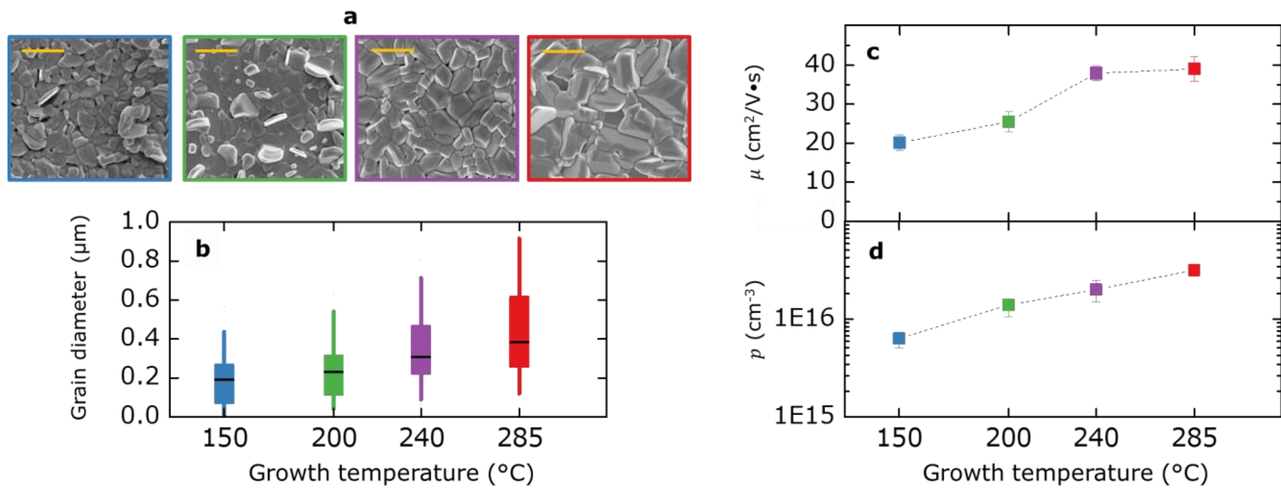

Figure 1. Experimental data on structural and electrical properties. (a) Plan-view SEM, showing increasing grain size with growth temperature (increasing temperature left to right: 150°C in blue, 200°C in green, 240°C in purple, 285°C in red). Scale bar indicates 1 μm. (b) Distribution of post-annealed grain diameters tending towards larger grains with increasing growth temperature. Black horizontal line indicates median; edges of box indicate 25th and 75th percentiles; whiskers indicate 5th and 95th percentiles. (c),(d) Hall mobility and carrier concentration, respectively, both increasing with growth temperature. Error bars indicate propagation of experimental uncertainty in thickness measurement by SEM and contact placement.

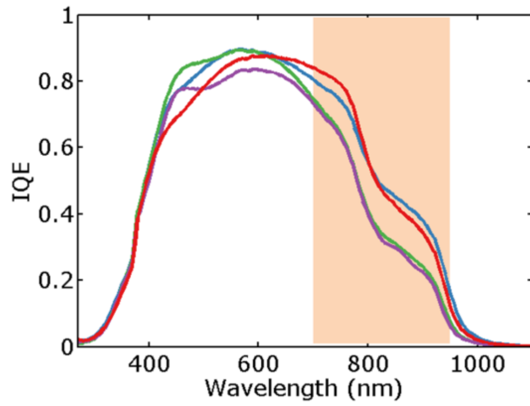

Figure 2. Measured internal quantum efficiency of SnS thin-film devices for the four growth temperatures (150°C in blue, 200°C in green, 240°C in purple, 285°C in red). The highlighted region indicates the wavelength range (700–950 nm) which was fitted using a one-dimensional opto-electronic model in SCAPS-1D.

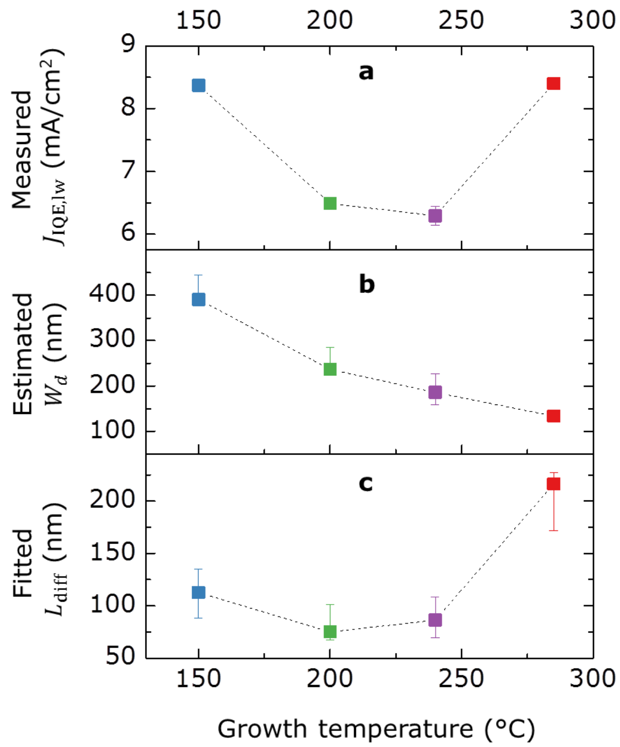

Figure 3. SnS thin-film device parameters as a function of growth temperature (150°C in blue, 200°C in green, 240°C in purple, 285°C in red). (a) Current density $J_{\mathrm{IQE,lw}}$ extracted from experimental IQE by integrating over the long-wavelength regime (700–950 nm). (b) Estimated depletion width W_d based on the measured hole concentration. Error bars represent uncertainty in material parameter values. (c) Fitted diffusion length L_{diff} based on a one-dimensional opto-electronic model in SCAPS-1D. Error bars take into account both uncertainty in material parameters from the literature, as well as the effect of varying T_{g}-dependent parameters other than hole concentration.

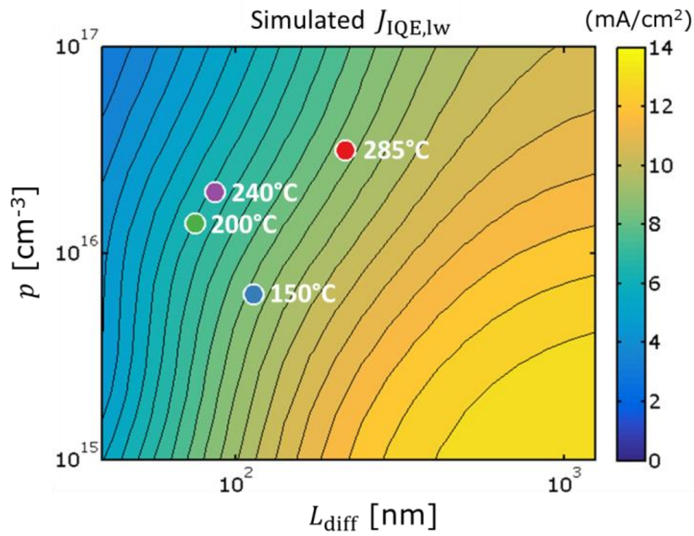

Figure 4. Contour plot of the current density $J_{\mathrm{IQE,lw}}$ as a function of diffusion length L_{diff} (abscissa) and hole concentration p (ordinate). The experimental data points representing each growth temperature are positioned based on measured carrier concentration and fitted diffusion length. Within the parameter space plotted, lower p and higher L_{diff} tend to increase $J_{\mathrm{IQE,lw}}$.

References

[1] K. Ramakrishna Reddy, N. Koteswara Reddy, and R. Miles, Sol. Energy Mater. Sol. Cells **90**, 3041 (2006).

[2] P. Sinsermsuksakul, J. Heo, W. Noh, A.S. Hock, and R.G. Gordon, Adv. Energy Mater. **1**, 1116 (2011).

[3] A. Tanusevski and D. Poelman, Sol. Energy Mater. Sol. Cells **80**, 297 (2003).

[4] K. Hartman, J.L. Johnson, M.I. Bertoni, D. Recht, M.J. Aziz, M. a. Scarpulla, and T. Buonassisi, Thin Solid Films **519**, 7421 (2011).

[5] V. Steinmann, R. Jaramillo, K. Hartman, R. Chakraborty, R.E. Brandt, J.R. Poindexter, Y.S. Lee, L. Sun, A. Polizzotti, H.H. Park, R.G. Gordon, and T. Buonassisi, Adv. Mater. **26**, 7488 (2014).

[6] H. Noguchi, A. Setiyadi, H. Tanamura, T. Nagatomo, and O. Omoto, Sol. Energy Mater. Sol. Cells **35**, 325 (1994).

[7] A. Schneikart, H.-J. Schimper, A. Klein, and W. Jaegermann, J. Phys. D. Appl. Phys. **46**, 305109 (2013).

[8] T. Ikuno, R. Suzuki, K. Kitazumi, N. Takahashi, N. Kato, and K. Higuchi, Appl. Phys. Lett. **102**, 193901 (2013).

[9] P. Sinsermsuksakul, K. Hartman, S. Bok Kim, J. Heo, L. Sun, H. Hejin Park, R. Chakraborty, T. Buonassisi, and R.G. Gordon, Appl. Phys. Lett. **102**, 053901 (2013).

[10] H.H. Park, R. Heasley, L. Sun, V. Steinmann, R. Jaramillo, K. Hartman, R. Chakraborty, P. Sinsermsuksakul, D. Chua, T. Buonassisi, and R.G. Gordon, Prog. Photovoltaics Res. Appl. **20**, (2014).

[11] P. Sinsermsuksakul, L. Sun, S.W. Lee, H.H. Park, S.B. Kim, C. Yang, and R.G. Gordon, Adv. Energy Mater. **4**, (2014).

[12] S. Siebentritt, Sol. Energy Mater. Sol. Cells **95**, 1471 (2011).

[13] C.. Ferekides, D. Marinskiy, V. Viswanathan, B. Tetali, V. Palekis, P. Selvaraj, and D.. Morel, Thin Solid Films **361-362**, 520 (2000).

[14] W.N. Shafarman and J. Zhu, Thin Solid Films **361**, 473 (2000).

[15] M. Devika, N. Koteeswara Reddy, D. Sreekantha Reddy, Q. Ahsanulhaq, K. Ramesh, E.S.R. Gopal, K.R. Gunasekhar, and Y.B. Hahn, J. Electrochem. Soc. **155**, H130 (2008).

[16] M. Devika, K.T. Ramakrishna Reddy, N. Koteeswara Reddy, K. Ramesh, R. Ganesan, E.S.R. Gopal, and K.R. Gunasekhar, J. Appl. Phys. **100**, 023518 (2006).

[17] Y. Guo, W. Shi, Y. Zhang, L. Wang, and G. Wei, Proc. SPIE **6984**, 69841P (2008).

[18] R.W. Miles, O.E. Ogah, G. Zoppi, and I. Forbes, Thin Solid Films **517**, 4702 (2009).

[19] P. a. Nwofe, K.T.R. Reddy, G. Sreedevi, J.K. Tan, I. Forbes, and R.W. Miles, Energy Procedia **15**, 354 (2012).

[20] *See Supplementary Material at [doi] for Justification of 1-D Model and Details on Material Parameter Values.* (n.d.).

[21] R. Jaramillo, V. Steinmann, C. Yang, K. Hartman, R. Chakraborty, J.R. Poindexter, M.L. Castillo, R. Gordon, and T. Buonassisi, J. Vis. Exp. (2015).

[22] M.D. Abràmoff, P.J. Magalhães, and S.J. Ram, Biophotonics Int. **11**, 36 (2004).

[23] J. Vidal, S. Lany, M. d'Avezac, A. Zunger, A. Zakutayev, J. Francis, and J. Tate, Appl. Phys. Lett. **100**, 032104 (2012).

[24] J.W. Orton and M.J. Powell, Reports Prog. Phys. **43**, 1263 (1980).

[25] R. Scheer and H.-W. Schock, *Chalcogenide Photovoltaics: Physics, Technologies, and Thin Film Devices* (Wiley-VCH, 2011).

[26] M. Burgelman, P. Nollet, and S. Degrave, Thin Solid Films **361**, 527 (2000).

[27] H.C. Card and E.S. Yang, IEEE Trans. Electron Devices **24**, 397 (1977).

Supplemental material

Non-monotonic effect of growth temperature on carrier collection in SnS solar cells

R. Chakraborty,[1] V. Steinmann, [1] N. M. Mangan, [1] R. E. Brandt, [1] J. R. Poindexter, [1] R. Jaramillo, [1] J. P. Mailoa, [1] K. Hartman, [1] A. Polizzotti, [1] C. Yang, [2] R. G. Gordon, [2] T. Buonassisi,[1]

[1]*Massachusetts Institute of Technology, Cambridge, MA, 02139, USA*

[2]*Harvard University, Cambridge, MA, 02138, USA*

Grain size analysis

Visible grain boundaries in each plan-view SEM (one for each growth temperature) are manually traced using the raster graphics editor GIMP.[1] Each trace is processed using the "Analyze Particles" feature of the image analysis software ImageJ[2] to produce a list of in-plane grain areas $A_i$in units of pixel^2. Grain areas are converted to μm^2 using the scale bar on each SEM with systematic error ± 0.04 μm^2. The number of traced grains is $n > 120$ for each growth temperature. Using the simplifying assumption of circular grains, we plot the distribution of grain diameters $d_i = 2(A_i/\pi)^{1/2}$ for each growth temperature in Figure 1b.

SnS morphology vs. growth temperature on Si/SiO$_2$ substrates

Figure S1 shows plan-view SEMs of SnS grown on Si/SiO$_2$ substrates for each growth temperature. Similar to SnS grown on Si/SiO$_2$/Mo, SnS grown on Si/SiO$_2$ exhibits increasing grain size with growth temperature. However, we note that in general, the absolute grain sizes and morphology of SnS films on Si/SiO$_2$ are not identical to those on Si/SiO$_2$/Mo. Therefore, we may expect differences between the measured SnS hole mobility (via Hall effect on Si/SiO$_2$ substrates) and the SnS hole mobility for films grown on Mo which are used for devices. For this reason, we ensure that our IQE analysis does not use the measured carrier mobility on Si/SiO$_2$ substrates as an input. We use $L_{\text{diff}} = \sqrt{\frac{kT}{q}\mu_e\tau_n}$ as our effective fitting parameter, and within the explored parameter space, the minority-carrier mobility μ_e

and minority-carrier lifetime τ_n affect $J_{\mathrm{IQE,lw}}$ equivalently. Thus, μ_e is not used as an input to the simulations; rather, it is wrapped into the effective fitting parameter.

Although the IQE analysis does not rely on the measured μ_e, it does rely on the measured hole concentration p, which is also measured via Hall effect on Si/SiO_2 substrates. However, the conclusion that L_{diff} increases at the highest growth temperature of 285°C depends on the *trend* in carrier concentration with growth temperature rather than the absolute values of carrier concentrations. Since we see a similar trend in SnS film morphology on Si/SiO_2 as on Si/SiO_2/Mo substrates, we expect a similar trend in hole concentration between the two substrates as a function of growth temperature.

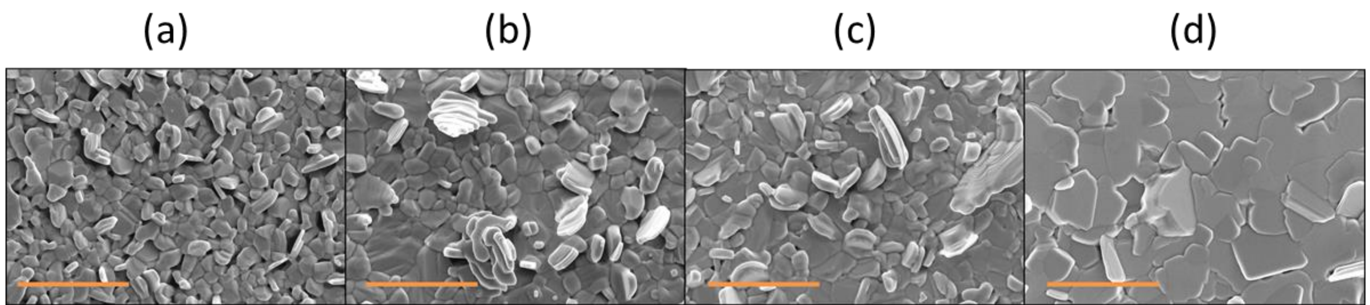

Figure S1. Scanning electron micrographs of post-annealed Si/SiO_2/SnS for each growth temperatures. (a) 150°C; (b) 200°C; (c) 240°C; (b) 285°C. Scale bar indicates 1 μm.

SnS film thickness

The SnS film thicknesses on Si/SiO_2/Mo are measured by cross-sectional SEM. Figure S2 shows the measured thickness of as-deposited and annealed SnS films for each growth temperature, with error bars representing the standard deviation of surface roughness as measured by atomic force microscopy (see next section). We observe that for each growth temperature, annealing does not change the film thickness to within error. Re-evaporation is strongly suppressed during annealing presumably because of the high total pressure (28 torr). The post-annealed film thicknesses range from 886-1204 nm due to differences in surface topology and error in deposition rate measurement.

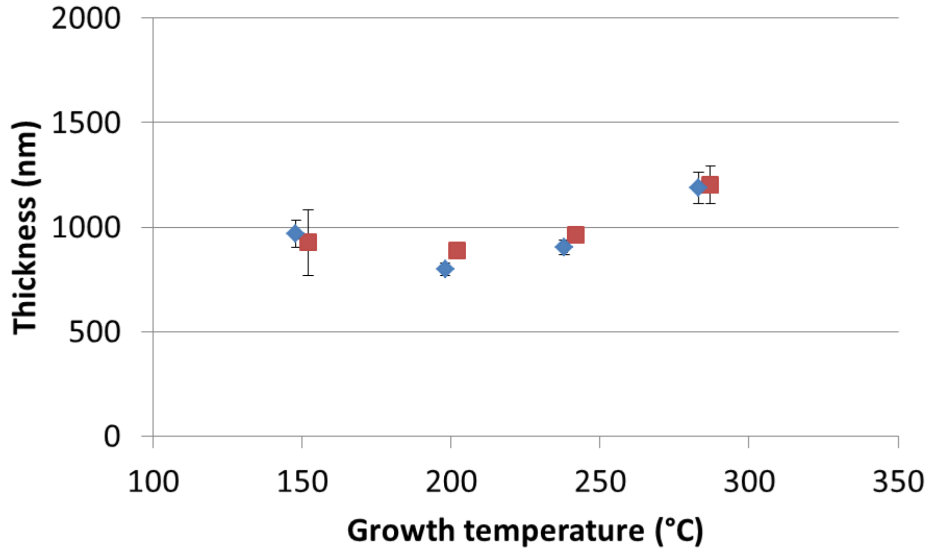

Figure S2. Data points indicate the SnS film thickness as measured by cross-sectional SEM of as-deposited (red squares) and annealed (blue diamonds) samples, respectively. The error bars represent the standard deviation of surface roughness as measured by AFM over one 2x2 μm^2 area on each sample.

Variation in absorption due to surface roughness

As shown by the atomic force microscopy (AFM) scans in Figure S3, the structure of the SnS surface changes with growth temperature. Surface topology may affect carrier collection in that high-aspect-ratio surface structures tend to lower the average distance from the bulk to the junction. Note that this mechanism is different from surface roughness leading to decreased reflectance, of which IQE is independent. The root-mean-squared roughness for the post-annealed samples are shown in Figure S4. Although the trend in roughness roughly mirrors that of $J_{\mathrm{IQE,lw}}$, we find through two-dimensional optical simulations that the effect of surface topology on long-wavelength carrier collection is not sufficient to explain the magnitude of changes in $J_{\mathrm{IQE,lw}}$ versus growth temperature.

Topology data from AFM line scans are used to create a quantitatively accurate device cross-section. The device cross-section is fed into a finite-difference time-domain optical absorption simulation, resulting in a 2D normalized generation profile $G_n(x, y, \lambda)$ through the thickness of the device. Here,

$G_n(x, y, \lambda)$ is normalized to the incident photon flux used in the simulation such that $\iint G_n(x, y, \lambda)\, dx\, dy = 1$. The computed 2D normalized generation profile is then converted to a 1D normalized generation profile $G_n(w', \lambda)$ as a function of distance to the nearest junction w', such that $\int G_n(w', \lambda)\, dw' = 1$. In order to estimate the magnitude of the differences in $J_{\text{IQE,lw}}$ due to surface topology, we then integrate $G_n(w', \lambda)$ for long wavelengths up to a collection depth w to obtain a collection-depth-dependent current density

$$J_{\text{IQE,lw}}(w) = \int_0^w \int_{700\text{ nm}}^{950\text{ nm}} G(w', \lambda)\, \phi_{AM1.5}(\lambda)\, \frac{\lambda}{hc}\, d\lambda\, dw'.$$

The computed $J_{\text{IQE,lw}}(w)$ for each growth temperature is plotted in Figure S5

, along with a similarly computed $J_{\text{IQE,lw}}(w)$ for the case of a planar surface. All AFM-based simulations show enhanced $J_{\text{IQE,lw}}(w)$ relative to the planar case, indicating that we may be systematically overestimating the diffusion length in our films by assuming a planar surface. In addition, the range of $J_{\text{IQE,lw}}(w)$ due to surface topology alone – that is, for a given collection depth w – may account for up to 35% of the differences in measured $J_{\text{IQE,lw}}$ across samples. Although this effect is significant, a change in collection depth is still necessary to account for the majority of the variation in measured $J_{\text{IQE,lw}}$. Thus, we focus on the effect of carrier concentration and diffusion length as the main drivers of changes in long-wavelength carrier collection across our samples.

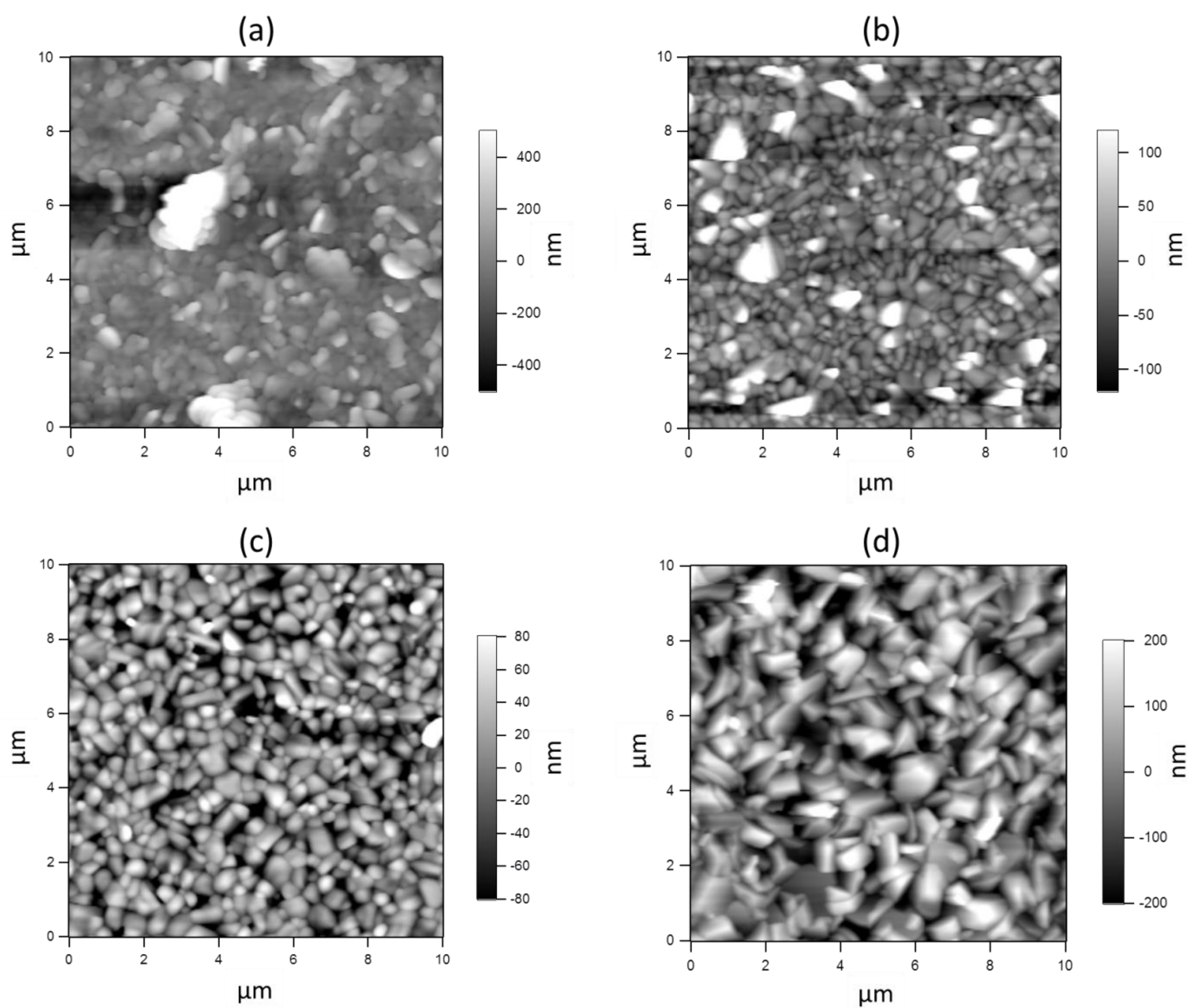

Figure S3. AFM scans of the post-annealed SnS films for each growth temperature. (a) 150°C; (b) 200°C; (c) 240°C; (b) 285°C. Note the changing surface morphology.

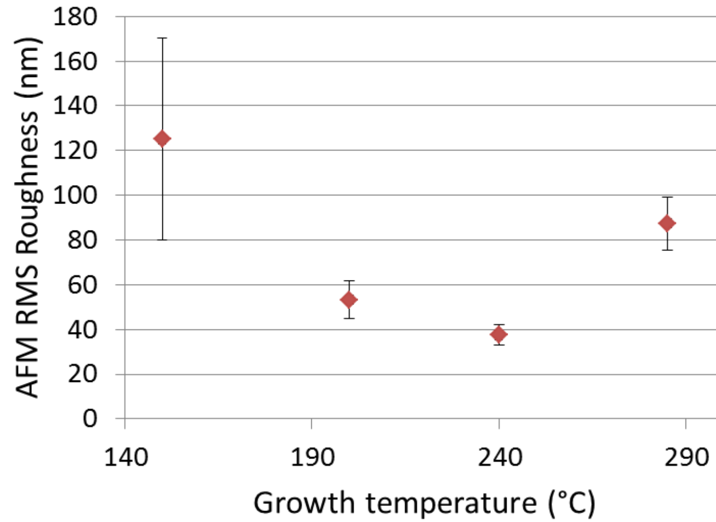

Figure S4. Root-mean-squared (RMS) surface roughness as measured by AFM for each post-annealed sample. Points and error bars represent the average and standard deviation of RMS roughness over 9 distinct 3x3 μm^2 areas on each sample, respectively.

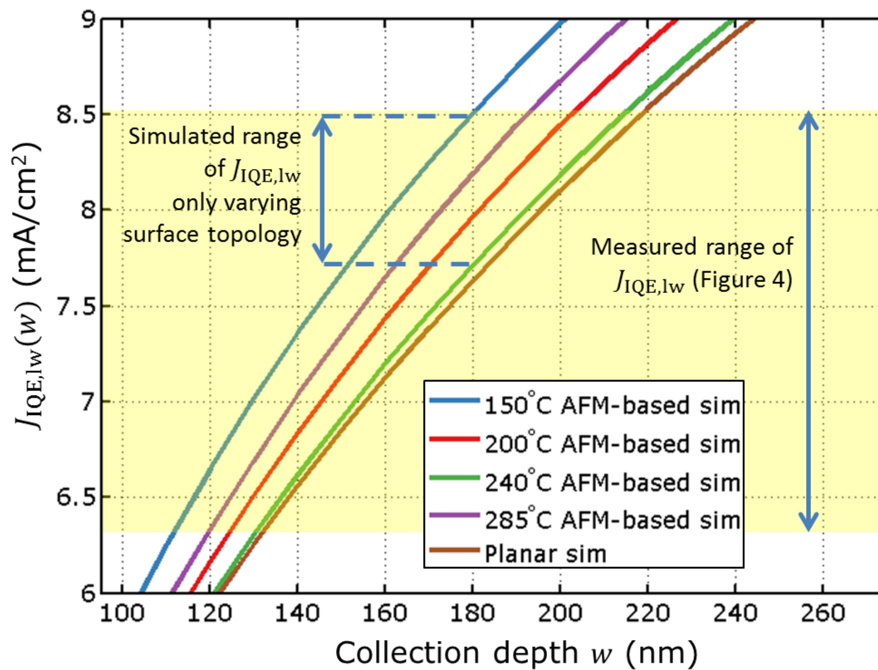

Figure S5. Collection-depth-dependent integrated IQE, simulated using a 2D AFM-based optical model for each post-annealed sample. The same simulation assuming a planar surface is also shown for comparison. All AFM-based simulations show enhanced $J_{\mathrm{IQE,lw}}(w)$ relative to the planar case. However, the difference in $J_{\mathrm{IQE,lw}}(w)$ across samples for a given collection depth w is not sufficient to account for the change in measured $J_{\mathrm{IQE,lw}}$, which ranges from 6.3-8.5 mA/cm^2.

Material parameter values assumed in simulations

The material parameter values listed in Table S1 define our numerical model. In addition to SnS hole concentration, which is measured directly for the current sample set (Figure 1c), four additional parameters vary with growth temperature: SnS hole mobility, electron mobility, SnS dielectric constant, and SnS/Zn(O,S):N conduction band offset. The upper and lower bounds in Table S1 for these additional parameters represent the expected variation across growth temperatures (see below for discussion of individual parameters). The remaining properties are held constant across growth temperatures, and the upper and lower bounds denote experimental uncertainties.

The fitted diffusion lengths denoted by the filled squares in Figure 3c use the best-estimate material parameter values from Table S1. The error bars in Figure 3c represent the upper and lower bounds for the fitted L_{diff} using all permutations of the upper and lower bounds from Table S1.

Material parameter	Best estimate	Lower bound	Upper bound	Source
SnS thickness	1000 nm	-	-	SEM cross-section
SnS bandgap	1.1 eV	-	-	[3]
SnS dielectric constant	T_g-dependent: see Table S2.	37	43	[4], XRD for anisotropic correction
SnS h^+(e^-) mobility	T_g-dependent: see Figure 1c.	20 (32) $cm^2/V{\cdot}s$	40 (115) $cm^2/V{\cdot}s$	Hall effect (m_h^*/m_e^* from [3])
SnS h^+ carrier density	T_g-dependent: see Figure 1d.	See Figure 1d, lower error bar.	See Figure 1d, upper error bar.	Hall effect
SnS optical absorption coefficient	Measured for $T_g = 240°C$.	-	-	[5]
SnS h^+(e^-) effective mass	0.68 (0.28) m_0	-	-	[3]
SnS valence (conduction) band density of states	3.6e18 (1.4e19) cm^{-3}			from effective mass
SnS/Zn(O,S):N conduction band offset ($\chi_{SnS} - \chi_{ZnOS}$)	T_g-dependent: see Table S3.	-0.53	-0.33	[3,6], XRD for anisotropic correction
SnS/Zn(O,S):N interface recombination velocity	1e4 cm/s	0 cm/s	1e5 cm/s	[6]
Zn(O,S):N thickness	30 nm	-	-	[5]
Zn(O,S):N e^- carrier density	5.3e13 cm^{-3}	2.4e13 cm^{-3}	2.4e14 cm^{-3}	[6]
Zn(O,S):N, ZnO dielectric constant	9	-	-	[7]
Zn(O,S):N, ZnO h^+(e^-) effective mass	2.0 (0.19) m_0	-	-	[8]
Zn(O,S):N, ZnO valence (conduction) band density of states	7.0e19 (2.0e18) cm^{-3}	-	-	from effective mass
ZnO thickness	10 nm	-	-	[5]
ZnO e^- carrier density	1e19 cm^{-3}	-	-	[9,10]
ZnO electron affinity	4.28 eV	-	-	[11]
ITO, ZnO, Zn(O,S):N bandgaps	> 2.5 eV	-	-	[6]

Table S1. Material parameter values for device layers assumed in electronic simulations. Note that the best estimates for SnS dielectric constant, hole and electron mobility, hole carrier density, and SnS/Zn(O,S):N conduction band offset vary with growth temperature; for these parameters, the upper and lower bounds represent the range of values expected across growth temperatures. All other material parameters are assumed to be constant with growth temperature; for these parameters, the upper and lower bounds represent uncertainty in the literature value. Values for the Zn(O,S):N carrier concentration are from measurements performed in the dark.

SnS dielectric constant

The dielectric constant in SnS is known to be significantly anisotropic as measured on single crystals.[12] For the purpose of the simulation, we are interested in the dielectric constant in the direction of carrier transport, which is perpendicular to the substrate (out-of-plane). For any particular grain in a polycrystalline film, the dielectric constant in the out-of-plane direction depends on the particular orientation of that grain. We estimate the effective out-of-plane dielectric constant for our polycrystalline films by taking a weighted average of the orientation-dependent dielectric constant based on the grain orientation distribution as measured by X-ray diffraction (XRD).

XRD is taken on each post-annealed sample in Bragg-Brentano configuration in the range 20-60°2θ. Within this range, at least 13 peaks corresponding to orthorhombic SnS (ICDD 00-039-0354) are identified for each sample. The degree of preferred orientation is computed using the fiber texture method,[13] in which the volume fraction f_{hkl} of crystals oriented with $(h\ k\ l)$ parallel to the substrate is determined by

$$f_{hkl} = \frac{I_{hkl}/I'_{hkl}}{\sum I_{hkl}/I'_{hkl}}$$

where I_{hkl} is the measured peak intensity of the film, and I'_{hkl} is the reference peak intensity of a randomly oriented sample (ICDD 00-039-0354). We assume that the set of >13 measured peaks gives a representative distribution of grain orientations for the film.

Using Miller index notation, let $[h'\ k'\ l']$ be the unit normal vector to the set of planes $(h\ k\ l)$. The dielectric constant in the direction of the unit normal vector is given by[14]

$$\epsilon_{hkl} = h'^2\epsilon_{11} + k'^2\epsilon_{22} + l'^2\epsilon_{33}$$

where ϵ_{11}, ϵ_{22}, and ϵ_{33} are the diagonal elements of the dielectric constant tensor for SnS. These tensor components have been measured in the literature via spectroscopic ellipsometry on SnS single crystals, and range from 34.06 to 51.66.[12] Lastly, we estimate the effective out-of-plane dielectric constant as the weighted average

$$\epsilon_{\text{eff}} = \sum_{hkl} f_{hkl}\epsilon_{hkl}.$$

The computed values of ϵ_{eff} range from 37.9-42.1 and are listed in Table S2 for each growth temperature. These values are used as inputs to the simulation to obtain the fitted diffusion lengths represented by the filled squares in Figure 3C. However, we note that the variation in ϵ_{eff} alone is insufficient to produce the observed trend in $J_{\text{IQE,lw}}$; in fact, the variation in ϵ_{eff} as a function of growth temperature produces a maximum in $J_{\text{IQE,lw}}$ at $T_{\text{g}} = 240°\text{C}$, which is the opposite behavior to that measured. The insensitivity of the fitted diffusion length to ϵ_{eff} is shown by the error bars in Figure 3c, which include the variation of fitted diffusion length due to the variation of ϵ_{eff} within the calculated range. Thus, even with varying ϵ_{eff} in the range 37.9-42.1 for all growth temperatures, the measured $J_{\text{IQE,lw}}$ at the highest growth temperature of 285°C cannot be explained without an increase in diffusion length.

Growth temperature (°C)	150	200	240	285
ϵ_{eff}	39.7	41.3	42.1	37.9

Table S2. Computed values of ϵ_{eff} for each post-annealed sample based on the volume fractions of grain orientations measured by XRD.

SnS hole and electron mobility

We use the measured SnS Hall mobility (Figure 1c) as the SnS hole mobility in our simulations. Although the Hall mobility is measured in the plane of the thin film, we find that taking anisotropy into account is not necessary in the parameter regime defined by Table S1. In this parameter regime, the electron mobility μ_e does not affect the simulation separate from the electron lifetime τ_e, as only terms with $\mu_e\tau_e$ as a product are dominant.

The mobility for carriers of type i can be expressed as $\mu_i = q\tau_{c,i}/m_i^*$, where q is the electron charge, $\tau_{c,i}$ is the collision time, and m_i^* is the effective mass of carrier type i.[15] We assume equal collision

times between holes and electrons and obtain the electron mobility by multiplying the hole mobility by a factor m_h^*/m_e^*, where the effective masses are listed in Table S1.

SnS optical absorption

The long-wavelength optical absorption coefficient for a SnS film grown on glass at 240°C and similarly annealed has been measured and previously published.[5] This absorption coefficient was held constant as a function of growth temperature in the simulations. However, we note that like dielectric constant, the absorption coefficient is also anisotropic. Therefore, as a check, we perform an analogous calculation as for dielectric constant to obtain an effective weighted-average absorption coefficient based on the volume fractions of orientations measured by XRD for each sample. For this calculation, we extract the anisotropic extinction coefficient from spectrally resolved anisotropic optical measurements from the literature.[12] For each growth temperature, we re-fit the diffusion length using the modified absorption coefficient calculated for that growth temperature, along with best-estimate values of other material parameters listed in Table S1. The results are shown in Figure S6; the two points for each growth temperature represent the limits of fitted L_{diff} obtained by varying the SnS carrier concentration between the lower and upper bounds defined in Table S1. Although the absolute value of L_{diff} decreases from that in Figure 3c, the trends still hold; an increase in diffusion length at $T_{\mathrm{g}} = 285°\mathrm{C}$ is still necessary to explain the long-wavelength IQE enhancement at that temperature.

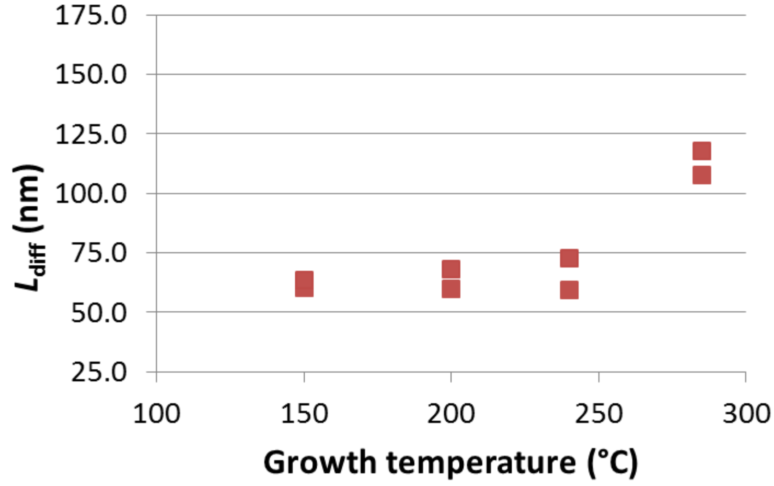

Figure S6. Re-fitted diffusion lengths using modified orientation-dependent absorption coefficient for each sample. The two points for each growth temperature indicate the limits of fitted diffusion length obtained by varying the SnS carrier concentration between the lower and upper bounds defined in Table S1. The trend of near-constant L_{diff} for $T_{\text{g}} < 285°\text{C}$ and an increase in L_{diff} still holds.

Effective mass and density of states

SnS hole and electron effective masses m_h^* and m_e^* are taken by averaging the anisotropic effective masses calculated in the literature.[3] The valence and conduction band density of states are then calculated by

$N_{\text{V}} = 2\left(\frac{2\pi m_h^* k_B T}{h^2}\right)^{3/2}$ and $N_{\text{C}} = 2\left(\frac{2\pi m_e^* k_B T}{h^2}\right)^{3/2}$, respectively, where k_B is the Boltzmann constant, h is the Planck constant, and $T = 297$ K.

ZnO hole and electron effective masses are similarly taken by averaging anisotropic effective masses in the literature,[8] and the valence and conduction band density of states are calculated in the same way. We assume that the effective mass and density of states for ZnO are equal to those of Zn(O,S):N.

SnS/Zn(O,S):N conduction band offset

The conduction band offset (CBO) at the SnS/Zn(O,S) interface has been measured using combined X-ray photoelectron and optical absorption measurements.[6] This measurement was performed for a SnS film grown at 240℃ and similarly annealed. Again we must address the issue of anisotropy. The SnS electron affinity is predicted to vary with $(h\ k\ l)$,[16] which means the band offset at the SnS/Zn(O,S):N interface may change with grain orientation. Therefore, as a check, we perform an analogous calculation as for dielectric constant to obtain an effective weighted-average SnS electron affinity based on the volume fractions of orientations measured by XRD for each sample. For this calculation, the electron affinity for each crystal surface of SnS is taken from the literature.[16] We then compute the implied SnS/Zn(O,S):N CBO by using the measured value for the sample grown at 240°C as a reference, assuming that the Zn(O,S):N electron affinity is constant. Table S3 shows the computed values of SnS electron affinity and implied SnS/Zn(O,S):N conduction band offset for each sample.

The CBO values in Table S3 are used as inputs to the simulation to obtain the fitted diffusion lengths represented by the filled squares in Figure 3c. However, we note that the variation in CBO alone is insufficient to produce the observed trend in $J_{\mathrm{IQE,lw}}$. This is shown by the error bars in Figure 3c, which include the variation of fitted diffusion length due to the variation of the CBO within the calculated range. Thus, even with varying the CBO in the range -0.53 to -0.33 for all growth temperatures, the measured $J_{\mathrm{IQE,lw}}$ at the highest growth temperature of 285°C cannot be explained without an increase in diffusion length.

Growth temperature (°C)	150	200	240	285
χ_{SnS} (eV)	4.12	4.21	4.16	4.01
$\chi_{\mathrm{SnS}} - \chi_{\mathrm{ZnOS}}$ (eV)	-0.42	-0.33	-0.38*	-0.53

Table S3. Computed values of SnS electron affinity for each post-annealed sample based on the volume fractions of grain orientations measured by XRD. The conduction band offset is calculated using the measured value (denoted by the asterisk) as a reference.

Zn(O,S):N carrier concentration

The electron carrier density in our Zn(O,S):N layer has been measured using the Hall effect.[6]

SnS/Zn(O,S):N interface recombination velocity

The recombination velocity at the SnS/Zn(O,S):N interface has not been measured, but more comprehensive fitting of device data including current-voltage data has recently been done.[6] From this work, we obtain the best-estimate, upper bound, and lower bound values given in Table S1 for interface recombination velocity.

Fitting L_{diff} in SCAPS-1D

In SCAPS-1D the minority carrier lifetime τ_n is set by Shockley-Read-Hall recombination with a single, neutral mid-gap defect level.[17,18] We vary τ_n during fitting by varying the total defect density. The fitted diffusion length is then $L_{\mathrm{diff}} = \sqrt{\frac{kT}{q}\mu_e\tau_n}$, where μ_e is the electron mobility described in Table S1. We note that since only the fitted diffusion length $L_{\mathrm{diff}} = \sqrt{\frac{kT}{q}\mu_e\tau_n}$ is reported, our results are independent of the exact mechanism by which τ_n is controlled.

Depletion width calculations in Figure 3b

Depletion width is estimated using the analytic form for an absorber/buffer/window system with a fully depleted buffer, derived in [[19]]. The material parameters used for this calculation are the best-estimate values listed in Table S1.

Calculation of contour plot in Figure 4

The best-estimate values for T_g = 240°C were used to compute the contour plot in Figure 4. The salient features of the contour plot do not change by using the best-estimate values for other growth temperatures, so we overlay the experimental data points for each growth temperature based on the measured carrier concentrations and fitted diffusion lengths.

Further experimental details

Atomic force microscopy measurements were carried out using an Asylum MFP-3D instrument in tapping mode and Olympus AC160-TS probes. The roughness was calculated from images with a 10 x 10 um^2 field of view.

Finite-difference time-domain (FDTD) optical absorption modeling was done by randomly choosing 5 scan lines out of the 256x256 point (10x10 μm^2) SnS texture obtained using AFM. For each of these scan lines, the texture of the subsequent layers grown using ALD (30 nm ZnOS14 and 10 nm AZO) was modeled by extending the SnS texture by 30 nm and 40 nm in perpendicular direction, while the texture of the sputtered ITO (250 nm thick) was modeled by growing the AZO texture in the vertical direction. These texture models were combined with the refractive index data of the material layers to construct the full FDTD model (Lumerical FDTD Solutions package). Afterwards, a 2-dimensional FDTD simulation was performed on each model (fixed mesh sizes of 5 nm in the horizontal direction and 2 nm in the vertical direction, electric field distribution $E(x,y)$ was recorded for wavelength range λ = 700-950

nm with wavelength step $\Delta\lambda$ of 10 nm), allowing us to calculate the spectrally-resolved generation profile $G(x,y,\lambda)$ for each of the 5 randomly chosen scan lines, which are then used in the IQE fitting simulation.

The texture of SnS films on Si/SiO_2/Mo substrates were analyzed by X-ray diffraction (XRD) on a Rigaku SmartLab with Cu $K\alpha$ radiation in Bragg-Brentano configuration in the 2θ range 20-60°.

References for Supplementary Materials

[1]GIMP - The GNU Image Manipulation Program, www.gimp.org (2001-2015).

[2] M.D. Abràmoff, P.J. Magalhães, and S.J. Ram, Biophotonics Int. **11**, 36 (2004).

[3] J. Vidal, S. Lany, M. d'Avezac, A. Zunger, A. Zakutayev, J. Francis, and J. Tate, Appl. Phys. Lett. **100**, 032104 (2012).

[4] R.E. Banai, H. Lee, M. a. Motyka, R. Chandrasekharan, N.J. Podraza, J.R.S. Brownson, and M.W. Horn, IEEE J. Photovoltaics 1 (2013).

[5] V. Steinmann, R. Jaramillo, K. Hartman, R. Chakraborty, R.E. Brandt, J.R. Poindexter, Y.S. Lee, L. Sun, A. Polizzotti, H.H. Park, R.G. Gordon, and T. Buonassisi, Adv. Mater. **26**, 7488 (2014).

[6] N. Mangan, R.E. Brandt, V. Steinmann, R. Jaramillo, J.R. Poindexter, C. Yang, K. Hartman, R. Chakraborty, R.G. Gordon, and T. Buonassisi, *Framework to Predict Optimal Buffer-Layer Pairing with Tin Sulfide Solar Cell Absorbers: A Case Study for Zinc Oxysulfide* (2015).

[7] N. Ashkenov, B.N. Mbenkum, C. Bundesmann, V. Riede, M. Lorenz, D. Spemann, E.M. Kaidashev, a. Kasic, M. Schubert, M. Grundmann, G. Wagner, H. Neumann, V. Darakchieva, H. Arwin, and B. Monemar, J. Appl. Phys. **93**, 126 (2003).

[8] S.Z. Karazhanov, P. Ravindran, a. Kjekshus, H. Fjellvåg, U. Grossner, and B.G. Svensson, J. Appl. Phys. **100**, (2006).

[9] V. Quemener, M. Alnes, L. Vines, P. Rauwel, O. Nilsen, H. Fjellvåg, E. V Monakhov, and B.G. Svensson, J. Phys. D. Appl. Phys. **45**, 315101 (2012).

[10] H. Hejin Park, R. Heasley, and R.G. Gordon, Appl. Phys. Lett. **102**, 1 (2013).

[11] C. Persson, C. Platzer-Björkman, J. Malmström, T. Törndahl, and M. Edoff, Phys. Rev. Lett. **97**, 146403 (2006).

[12] R.E. Banai, L. a. Burton, S.G. Choi, F. Hofherr, T. Sorgenfrei, a. Walsh, B. To, a. Cröll, and J.R.S. Brownson, J. Appl. Phys. **116**, 013511 (2014).

[13] G.B. Harris, London, Edinburgh, Dublin Philos. Mag. J. Sci. **43**, 113 (1952).

[14] J.F. Nye, *Physical Properties of Crystals: Their Representation by Tensors and Matrices*, 2nd ed. (Clarendon Press, Glasgow, 1960).

[15] P. Wurfel, *Physics of Solar Cells*, 2nd editio (Wiley-VCH, 2010).

[16] V. Stevanović, K. Hartman, R. Jaramillo, S. Ramanathan, T. Buonassisi, and P. Graf, Appl. Phys. Lett. **104**, 211603 (2014).

[17] W. Shockley and W. Read, Phys. Rev. **87**, 835 (1952).

[18] R. Hall, Phys. Rev. **87**, 387 (1952).

[19] R. Scheer and H.-W. Schock, *Chalcogenide Photovoltaics: Physics, Technologies, and Thin Film Devices* (Wiley-VCH, 2011).

View publication stats